Available online at www.sciencedirect.com
ScienceDirect
Trans. Nonferrous Met. Soc. China 35(2025) 1075−1091
Transactions of Nonferrous Metals Society of China
www.tnmsc.cn

Microstructure evolution and mechanical properties of Mg−Gd−Zn alloy with and without LPSO phase processed by multi-directional forging

Jing-yi HUANG[1], Yao-ling LIU[1], Yu-xiang HAN[1], Ying-chun WAN[2], Chu-ming LIU[3], Zhi-yong CHEN[1]

1. School of Materials Science and Engineering, Central South University, Changsha 410083, China;
2. Light Alloy Research Institute, Central South University, Changsha 410083, China;
3. Hunan Meiyu Science and Technology Co., Ltd., Yueyang 414000, China

Received 5 September 2023; accepted 26 March 2024

Abstract: The homogenized Mg−5.6Gd−0.8Zn (wt.%) alloys were treated with water cooling and furnace cooling to obtain specimens without and with the 14H long-period stacking ordered (LPSO) phase. Subsequently, multi-directional forging (MDF) experiments were carried out. The microstructure and mechanical properties of different regions (the center, middle and edge regions) in the MDFed alloys were systematically investigated, and the effect of LPSO phase on them was discussed. The results show that the alloys in different regions undergo significant grain refinement during the MDF process. Inhomogeneous microstructures with different degrees of dynamic recrystallization (DRX) are formed, resulting in microhardness heterogeneity. The alloy with the LPSO phase has higher microstructure homogeneity, a higher degree of recrystallization, and better comprehensive mechanical properties than the alloy without the LPSO phase. The furnace-cooled alloy after 18 passes of MDF has the best comprehensive mechanical properties, with an ultimate compressive strength of 488 MPa, yield strength of 258 MPa, and fracture strain of 21.2%. DRX behavior is closely related to the LPSO phase and deformation temperature. The kinked LPSO phase can act as a potential nucleation site for DRX grains, while the fragmented LPSO phase promotes DRX nucleation through the particle-stimulated nucleation mechanism.

Key words: Mg−Gd−Zn alloy; multi-directional forging; LPSO phase; twinning; kink; dynamic recrystallization

1 Introduction

Magnesium (Mg) and its alloys have shown great potential in the aerospace, automotive, and electronic communication industries due to their low density, high specific strength and good electromagnetic shielding [1−3]. However, the drawbacks of relatively low strength, low cold workability, and poor corrosion resistance are considered as the Achilles heel of Mg alloys, which seriously limits their widespread applications [4,5]. To attain the desired excellent performance, two fundamental methods are generally adopted to develop advanced Mg alloys: alloying [6] and appropriate forming processes [7]. From the alloying point of view, Mg−Gd based alloys are considered as one of the most promising candidates owing to their advanced strengths [8−10]. The Gd element has high solid solubility in magnesium, and the high-melting-point Mg_5Gd phase can be formed between Gd and Mg, which can realize the solid solution strengthening and aging strengthening of the alloy [11] and exhibit good mechanical properties at room temperature and high temperature. Furthermore, adding Zn element to the Mg−Gd based alloy in a certain proportion will promote the formation of the LPSO phase, which

Corresponding author: Zhi-yong CHEN, Tel: +86-13974926019, E-mail: czysh@netease.com
DOI: https://doi.org/10.1016/S1003-6326(24)66735-X

acts as a reinforcing phase and roughly coordinates with the short-fiber reinforcement mechanism, thereby further enhancing the strength and malleability of Mg alloys [12−14]. In recent years, the Mg−RE−Zn series alloys containing LPSO phases have attracted extensive attention due to their excellent comprehensive mechanical properties. WANG et al [15] investigated dynamic precipitation and microstructural evolution during hot deformation in a Mg−Zn−Gd alloy, and found that both the formation of 14H LPSO and dynamic precipitation of β'-Mg_7Gd should play a role in strengthening the $Mg_{97}Zn_1Gd_2$ alloy. In the work of LUAN et al [16], they studied the influence of the LPSO phase on the deformation mechanisms and tensile properties at elevated temperatures of the Mg−Gd−Zn−Mn alloys, and found that lamellar LPSO phase has a positive effect on strengthening the mechanical properties of the alloy, which is attributed to the hindrance of the LPSO phase to non-basal slip, the inhibitory function of kink to basal slip, and the inhibition of LPSO phase to discontinuous dynamic recrystallization (DDRX). Therefore, in this work, Mg−5.6Gd−0.8Zn (wt.%) alloy is taken as the experimental object to study.

Besides alloying, it has been found that the properties of Mg alloys can be greatly improved by means of severe plastic deformation (SPD), such as equal channel angular pressing (ECAP), multi-directional forging (MDF), accumulative roll bonding (ARB) and high-pressure torsion (HPT) [17−21]. Among the different SPD techniques, MDF is more capable of manufacturing relatively larger samples, which could be more appropriate for direct promotion in industrial production [22,23]. WANG et al [24] successfully fabricated Mg−8.0Gd−3.7Y−0.3Ag−0.4Zr (wt.%) bulk sample with exceptionally high strength by multi-directional forging (MDF) and subsequent ageing treatment. The forging−T5 sample (15 passes) exhibits room temperature mechanical properties of 391 MPa in yield strength, 448 MPa in ultimate tensile strength, and 3.9% in elongation to failure. The remarkable mechanical performance can be ascribed to the intensive grain refinement by the MDF process, dynamic precipitates, as well as precipitate strengthening by the β' phase.

However, MDF applied to Mg−Gd−Zn alloy containing the LPSO phase has been less reported. Besides, there is also no systematic comparison of the microstructure differences of Mg alloys with and without the 14H LPSO phase processed by MDF, and the degree and homogeneity of deformation during MDF processes show a great influence on the microstructure and mechanical properties. Therefore, the present work focuses on the effect of the LPSO phase on the microstructure evolution and mechanical properties of the Mg−Gd−Zn alloy during the MDF process. Particularly, the LPSO phase and its role in deformation and dynamic recrystallization (DRX) are emphatically discussed. In addition, the factors affecting the grain refinement and deformation mechanism are also proposed in this work.

2 Experimental

2.1 Material preparation

The experimental Mg−Gd−Zn alloy was prepared by semi-continuous casting and homogenization. Semi-continuous casting was carried out by melting pure Mg (99.99%), pure Zn (99.9%) and Mg−30wt.%Gd master alloy, using electric resistance furnace in SF_6 and CO_2 protective atmosphere. The composition of the ingot was determined to be Mg−5.6Gd−0.8Zn (wt.%) by an inductively coupled plasma (ICP) analyzer. The specimens cut from the central position of the cylindrical ingots were homogenized at 515 °C for 20 h. Some specimens were immediately quenched in water at 25 °C (referred to as the W alloy), while others were cooled in the furnace to 25 °C (referred to as the F alloy). The schematic diagram of the heat treatment process for the W and F alloys is revealed in Fig. 1(a).

2.2 Multi-directional forging (MDF)

Cubic specimens with dimensions of 40 mm × 40 mm × 40 mm of the W alloy and F alloy were subjected to MDF process. The MDF experiments were carried out at 450 and 500 °C, respectively, on a YA32−315 hydraulic forging machine with a limit load of 3150 kN. The forged samples were rotated by 90° after each pass to procure a "*X*-*Y*-*Z*-repeat" cyclical deformation (shown in Fig. 1(b)) to attain W-T450, F-T450, W-T500 and F-T500 alloy, where T450 and T500 imply the MDF temperatures (450 and 500 °C). The forging speed of the hammer was controlled at 15 mm/s, and the deformation amount of each pass

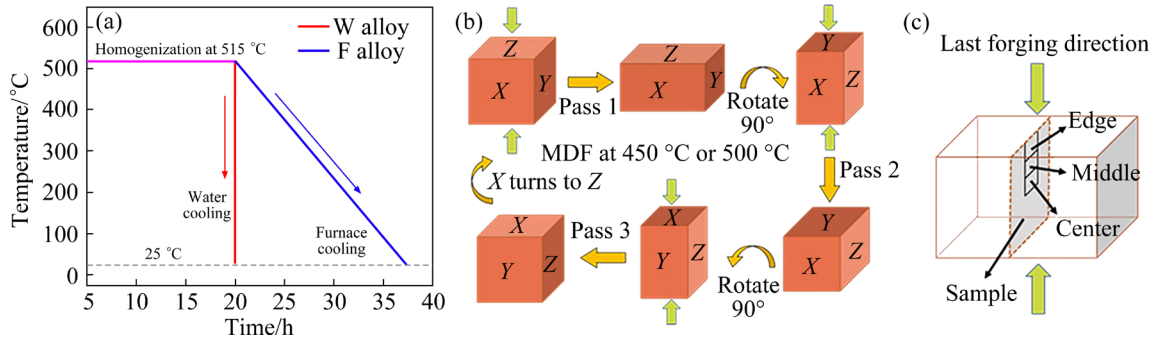

Fig. 1 Schematic diagram of heat treatment process (a); Schematic diagram of multi-directional forging (MDF) (b); Schematic diagram of sampling positions for microstructural observation and mechanical property tests (c)

was 15%. The MDFed samples were re-heated in a resistance furnace for 0.5 h to maintain the forging temperature of 450 and 500 °C, respectively, every 9 passes. Eventually, samples forged with 9 and 18 passes were obtained after water quenching.

2.3 Microstructure characterization

As shown in Fig. 1(c), the samples for microstructure characterization were subjected to electro-discharge machining from three different regions (center, middle, and edge regions) of the MDFed alloy bulk. The microstructure observation was performed using optical microscopy (OM) and scanning electron microscope (SEM, FEI Quanta 250 FEG) equipped with an electron backscatter diffraction (EBSD, FEI Helios Nanolab 600i) system. Microstructure observation at a finer level was obtained using a transmission electron microscope (TEM, FEI Titan G2 60−300) equipped with a field emission gun operating at 200 keV. Part of the TEM images were obtained in high-angle annular dark-field (HAADF-STEM) mode. Specimens for OM observation needed to be mechanically polished and corroded with an etching solution of 2.1 g picric acid, 5 mL glacial acetic acid, 5 mL distilled water, and 35 mL absolute ethanol. Specimens for SEM, EBSD, and TEM were prepared by mechanical polishing and electro polishing (twin-jet electro polishing for TEM samples) in a solution of absolute ethyl alcohol and 4% perchloric acid at −40 °C and 35 V. The phase analysis of the as-cast alloy and furnace-cooled alloy was carried out by a Rigaku D/Max 2500VB X-ray diffractometer (XRD), and the scanning parameters were in the range of 5°−80° with a speed of 8 (°)/min. All the XRD results were analyzed using MDI Jade 5 software. For the convenient description, the MDFed samples for microstructure characterization were designated as W-9P, F-9P, W-18P, and F-18P, where 9P and 18P imply the MDF passes.

2.4 Mechanical property tests

Compression samples with dimensions of *d*8 mm × 12 mm were machined from the center region of the MDFed samples, and the compression axis was parallel to the last forging direction (LD). Compression tests were carried out at ambient temperature on a standard universal testing machine (Instron 3369) with a constant loading speed of 0.5 mm/s. The compression yield strength (CYS) and ultimate compression strength (UCS) were obtained based on the average value of three reliable tests, and the results were averaged from three samples. Microhardness data of the MDFed alloys were collected using a Huayin HVS−1000 Vickers microhardness tester. The center, middle, and edge regions of each tested sample were drilled with 36 indentations (6 × 6 array, 108 indentations in total for each sample), respectively, using a constant loading of 9.8 N, and the holding time was set to be 15 s. The mechanical heterogeneity of the MDFed alloys was statistically evaluated by variance among the indentations.

3 Results

3.1 Initial microstructure

Figure 2 shows the XRD patterns of as-cast alloy and furnace-cooled alloy (F alloy). The results indicate that the as-cast alloy mainly consists of α-Mg matrix, $Mg_{12}ZnGd$ (LPSO phase), and Mg_5Gd phase. After homogenization at 515 °C for 20 h, the diffraction peak of Mg_5Gd phase is not detected in

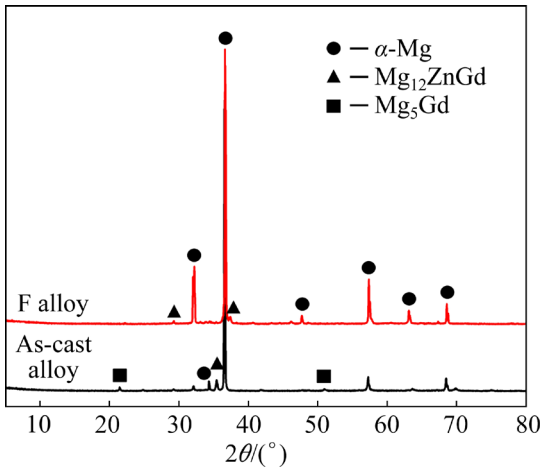

Fig. 2 XRD patterns of as-cast alloy and F alloy

the F alloy. The F alloy mainly consists of α-Mg matrix and $Mg_{12}ZnGd$ phase.

Figure 3 shows the microstructures of the as-cast and homogenized Mg−5.6Gd−0.8Zn (wt.%) alloy. As shown in Fig. 3(a), the light-colored area represents the α-Mg matrix in the as-cast alloy, while the dark part represents the second phase precipitated during the nonequilibrium solidification process. These network second phases are widely distributed within the grain and at the grain boundaries. Previous studies [25] have reported that the as-cast Mg−Gd−Zn alloy mainly consists of α-Mg and network eutectic Mg_5Gd phase. By combining these findings with the XRD results mentioned above, it can be determined that the network second phase in the as-cast alloy is the Mg_5Gd phase. After homogenization at 515 °C for 20 h, as shown in Figs. 3(b, c), the network eutectic phase is almost completely dissolved. The average grain sizes of the W alloy and F alloy are about 150 and 200 μm, respectively. Unlike the W alloy, the F alloy clearly shows densely arranged lamellar phases (seen in Fig. 3(d)) in the grain interior. These lamellar phases are LPSO phases, and they have the same orientation within a grain. The intragranular microstructure was further investigated by TEM, as shown in Figs. 3(e, f). The incident beam was parallel to $\langle 11\bar{2}0\rangle$. The selected area electron diffraction (SAED) pattern shows extra spots at $\pm n/7(0001)_{\alpha\text{-Mg}}$ (n is an integer), which indicates that the lamellar LPSO phases have a 14H-type stacking structure [2,3].

In order to further explore the black point phase in the W alloy (as shown in Fig. 3(b)) and the white short rod-like phase in the F alloy (as shown in Fig. 3(d)), SEM images of the W alloy and F alloy are shown in Fig. 4, and the corresponding EDS results are given in Table 1. According to Table 1, the point phase labeled A contains a large amount of Gd element, indicating that this phase is a rare earth rich phase. In addition to the lamellar LPSO phase precipitated in the grain, another second phase is observed at the grain boundary in Fig. 4(b). Compared with the second phase in the W

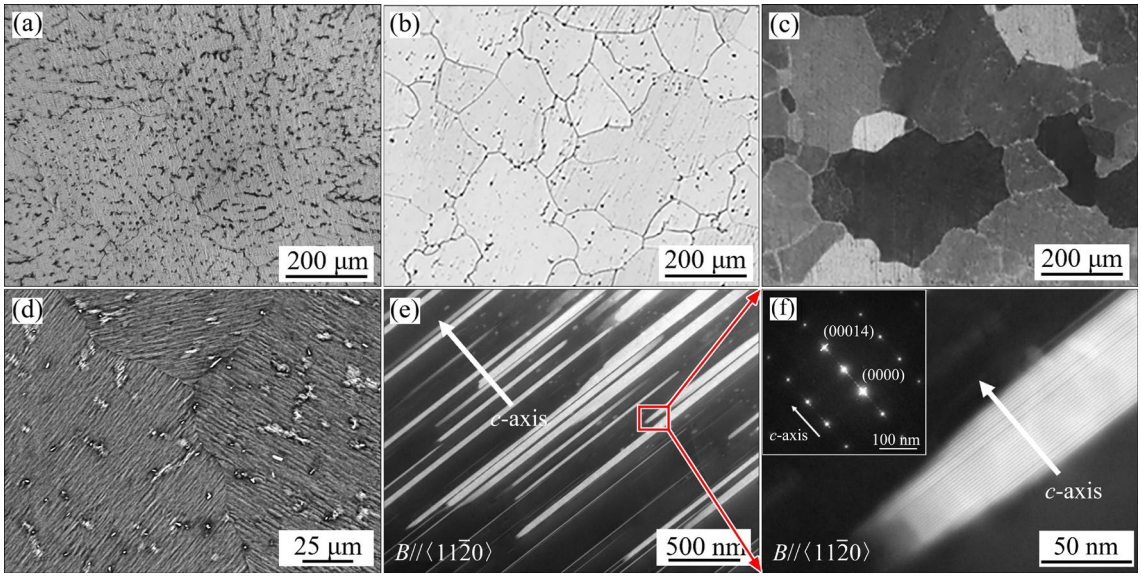

Fig. 3 Optical micrographs of as-cast (a), W (b) and F (c) alloys; SEM micrograph of F alloy (d); HAADF-STEM micrograph of F alloy (e); Higher magnified image of red rectangle area marked in (e) and corresponding typical SAED pattern of lamellar phase (f)

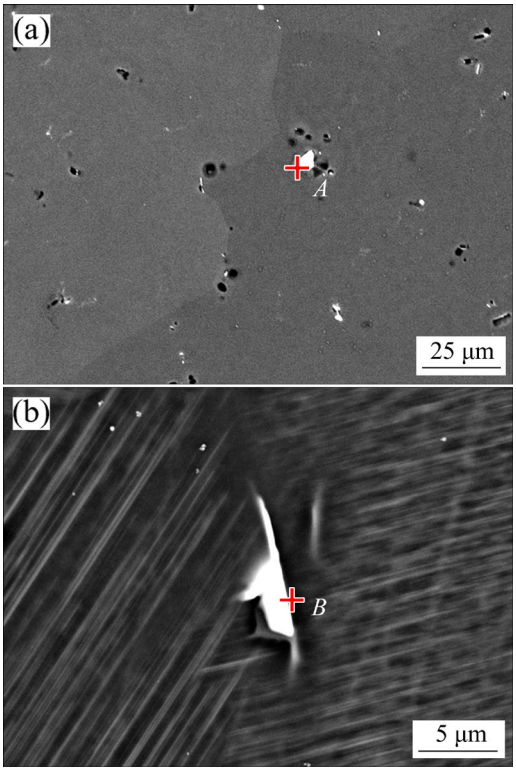

Fig. 4 SEM micrographs of W (a) and F (b) alloys

Table 1 Chemical compositions of EDS detection points in Fig. 4 (wt.%)

Point	Mg	Gd
A	21.09	78.91
B	60.42	39.58

alloy, the Gd element content of the second phase in the F alloy is reduced, which may be caused by the consumption of Gd by the precipitation of the LPSO phase.

3.2 Microstructure evolution during MDF process

Figure 5 shows the optical micrographs observed in W and F alloys, which exhibit the center, middle, and edge regions, respectively, in two alloys after 9 and 18 MDF passes. It can be seen that a large number of crisscross twins are detected in the W-9P sample (Figs. 5(a−c)), especially in the edge region, where the presence of DRX grains is hardly observed. The orientations of crystals in the homogenized alloy are relatively random, and the loading direction constantly changes in the process of MDF, which leads to the activation of twins in grains with different crystal orientations. In this case, the twinning should be the main deformation mode in the edge regions. The F-9P samples exhibit a similar situation (Figs. 5(d−f)), but they have a higher degree of DRX than W-9P samples evidently. Additionally, different regions of these samples exhibit different degrees of DRX. It is shown that the center region has the highest degree of DRX, followed by the middle region, while the edge region has the lowest degree of DRX.

When the MDF is increased to 18 passes, as shown in Figs. 5(g−i), the grains in the three regions of the above samples are further refined. DRX appears in the edge region, revealing necklace structures of small grains forming continuously along the boundaries of coarse grains. The degree of recrystallization in the middle region is further increased, and the remaining part of the coarse grains is not refined. The center region has a high degree of recrystallization, almost complete, which is composed of small DRX grains. At this time, there are still some differences in the microstructure of each region, but the uniformity of the microstructure is improved compared to that after 9 passes of deformation.

The degree of DRX gradually increases from the edge to the center of each sample, which is related to the inhomogeneous deformation of the samples during MDF process. It is noteworthy that the degree of recrystallization of the F alloy is higher than that of the W alloy at both 9 and 18 passes. In other words, the presence of the LPSO phase promotes the occurrence of DRX. The influence of the LPSO phase on the microstructure evolution of the alloy during MDF deformation may be attributed to the following two reasons. Firstly, the LPSO phase precipitated in the crystal obstructs the movement of dislocations, making it difficult for them to pass through the LPSO phase. This results in serious dislocation plugging and the release of stress through DRX. Secondly, a large amount of LPSO phases precipitated in the F alloy reduces the stacking fault energy. As a result, the proportion of energy release in the dynamic recovery process is very small, and high energy storage has a promoting effect on the DRX process.

Because of the relatively low degree of recrystallization in the edge region, the inverse pole figures (IPF) detected by EBSD in the edge region of W-9P, F-9P, W-18P and F-18P samples are shown in Figs. 6 and 7, with the reference direction

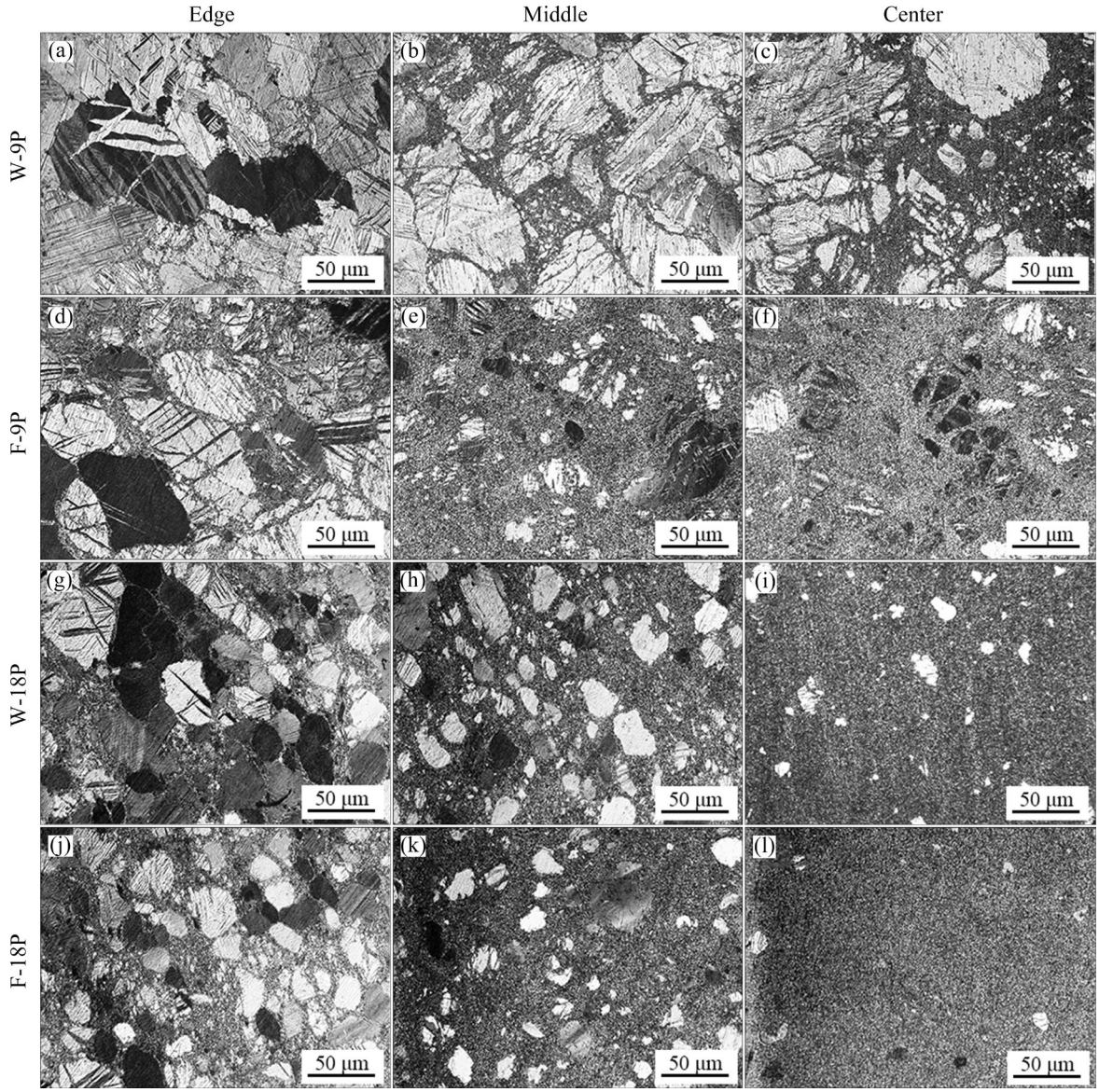

Fig. 5 Optical micrographs of MDFed Mg−Gd−Zn alloy in edge, middle and center regions

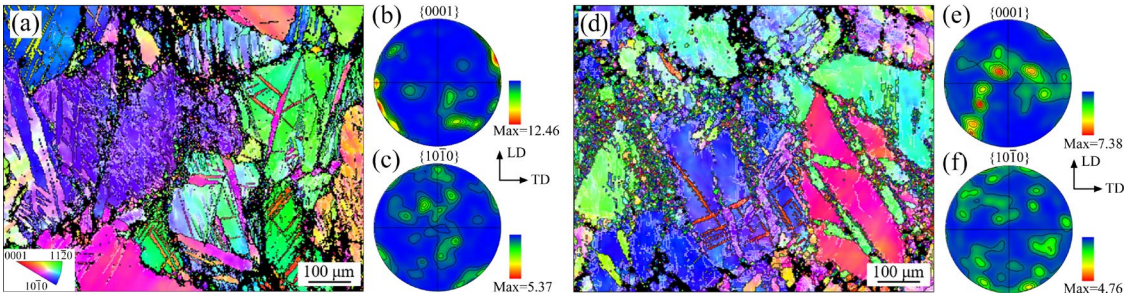

Fig. 6 Inverse pole figures (IPF) detected by EBSD (a, d) and corresponding {0001} (b, e) and {10$\bar{1}$0} (c, f) pole figures of MDFed Mg−Gd−Zn alloy after 9 passes: (a−c) W-9P sample; (d−f) F-9P sample

of the last forging direction (LD). As shown in Figs. 6(a, d), a large number of crisscross twins appear in the microstructure of both W-9P and F-9P alloys. It can be seen that twinning is the main deformation mode in the edge regions. The crystal orientation is deflected at a fixed angle due to twinning, changing from a sliding hard orientation to a sliding soft orientation. This promotes the operation of the new sliding system and indirectly coordinates the plastic deformation. Moreover, the

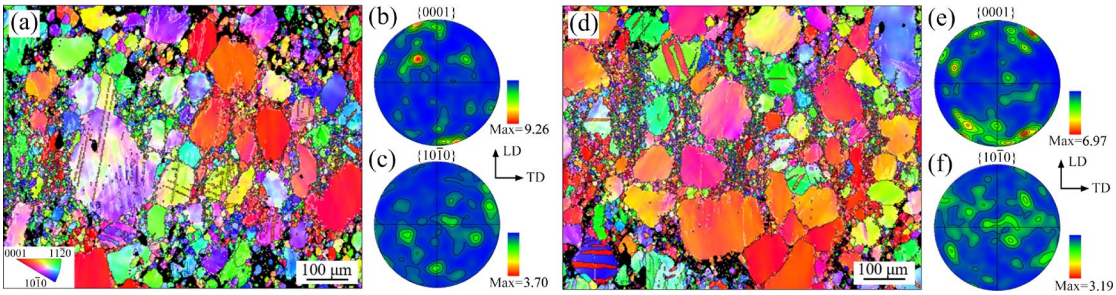

Fig. 7 Inverse pole figures (IPF) detected by EBSD (a, d) and corresponding {0001} (b, e) and {10$\bar{1}$0} (c, f) pole figures of MDFed Mg−Gd−Zn alloy after 18 passes: (a−c) W-18P sample; (d−f) F-18P sample

orientation of twins is random, and thus the changing loading direction of MDF is conducive to twins with different orientations. In addition, fine recrystallized grains are both observed in the grain boundaries of the W and F alloys. The fine recrystallized grains are banded in the W alloy, and the original coarse grains are refined due to DRX. As shown in the {0001} and {10$\bar{1}$0} pole diagrams in Fig. 6, the normal direction of the {0001} plane of the W alloy (i.e. the direction of the *c* axis) is concentrated near the TD direction. The polar density peaks of the F alloy are more dispersed in the LD−TD plane, and the maximum polar density is lower than that of the W alloy, which is caused by the higher degree of DRX in the F alloy.

As shown in Figs. 7(a, d), with MDF passes increased to 18 passes, there is a large number of DRX grains with a “necklace-like” distribution at the grain boundaries. Twins still appear in some large grains. The recrystallization fraction, averaged grain size and high angle grain boundaries (HAGBs, with a misorientation higher than 15°) of the MDFed samples are summarized in Table 2 (analyzed by Channel 5 software with uniform parameters). As given in Table 2, the degree of DRX increases substantially. The fraction of DRX grains in the W alloy increases from 2.63% to 7.46%. The original coarse grains are further refined to equiaxed grains, and the average grain size is refined from 5.03 to 4.55 μm. The fraction of HAGBs also increases from 45.73% to 47.43%. The F alloy shows the same tendency with an increase in forging passes, and the F-18P sample has the highest recrystallization fraction (10.91%) and the smallest averaged grain size (4.35 μm). As shown in the {0001} and {10$\bar{1}$0} pole diagrams in Fig. 7, the normal direction of the {0001} planes of W and F alloys is concentrated near the LD direction, and the pole density decreases compared to that of 9 passes. It can be seen that the constantly changing load direction of MDF helps weaken the concentrated distribution of crystal orientation. Additionally, the pole density of the F alloy with different passes is lower than that of the W alloy, which may be related to the existence of LPSO phase.

Table 2 Recrystallization fraction, averaged grain size and fraction of high angle grain boundaries (HAGBs, with misorientation higher than 15°) of MDFed samples

Sample	DRX fraction/%	Grain size/μm	HAGBs fraction/%
W-9P	2.63	5.03	45.73
F-9P	8.45	4.81	48.81
W-18P	7.46	4.55	47.43
F-18P	10.91	4.35	58.25

3.3 Mechanical properties

Figure 8 shows the hardness distribution at different regions of the samples after MDF. The figure provides the average hardness value for the entire sample and each region. There are differences in the microhardness among the three regions within the same sample, with the center region having the highest microhardness, followed by the middle region, and the edge region having the lowest microhardness. The fundamental reason for this phenomenon lies in the varying degree of deformation in each part, as well as the differences in the homogeneity of the microstructure and the average grain size. The center region experiences easy deformation, resulting in a high degree of deformation and DRX. As a result, the DRX grains in this region are relatively fine and uniform,

leading to the highest microhardness in the center region.

The W-18P sample has the lowest average microhardness of HV 82.01, while the average microhardness of MDFed alloy processed by 9−18 passes shows a weakening tendency. The change of the F alloy is similar, as the average microhardness declines from HV 89.18 in 9 passes to HV 83.88 in 18 passes. This indicates that as forging process continues, the degree of DRX increases and DRX softening occurs. The microhardness variance can represent the mechanical heterogeneity within the tested plane of a sample or a certain region. Among the four samples, the F-9P sample exhibits the least mechanical heterogeneity, with the lowest variance of 11.86, and its center microhardness value variance is as low as 7.42. With the increase of forging passes, the DRX degree and crushing degree of the LPSO phase are more different in three regions, and the mechanical heterogeneity is increased. Moreover, it can be inferred that the average hardness value of the F alloy is larger than the W alloy, regardless of whether it is after 9 passes or 18 passes, which may be related to load-bearing strengthening contributed by directionally arranged LPSO phase [26]. In conclusion, the development of microhardness heterogeneity of the MDFed alloy mentioned above should be theoretically attributed to the competition and balance of load-bearing strengthening, grain refinement, and DRX softening, among other factors.

To analyze the differences in mechanical properties between the W and F alloys after MDF and the variations in mechanical properties with different deformation passes more intuitively, Fig. 9 presents the engineering stress−strain curves and the bar charts depicting the yield strength, ultimate compressive strength, and fracture strain of the center region of the W and F alloys under 9 and 18

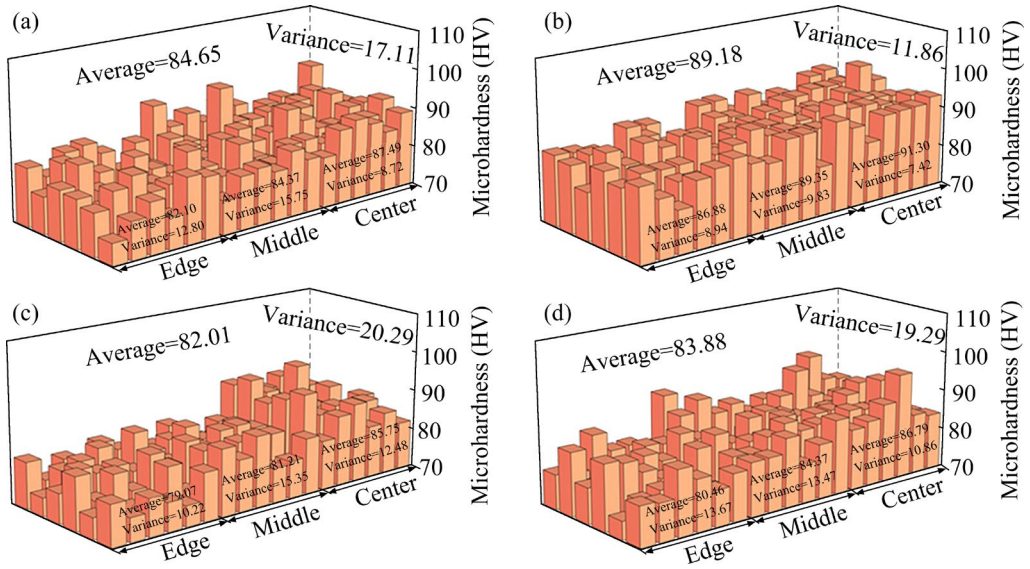

Fig. 8 Microhardness of W-9P (a), F-9P (b), W-18P (c) and F-18P (d) samples

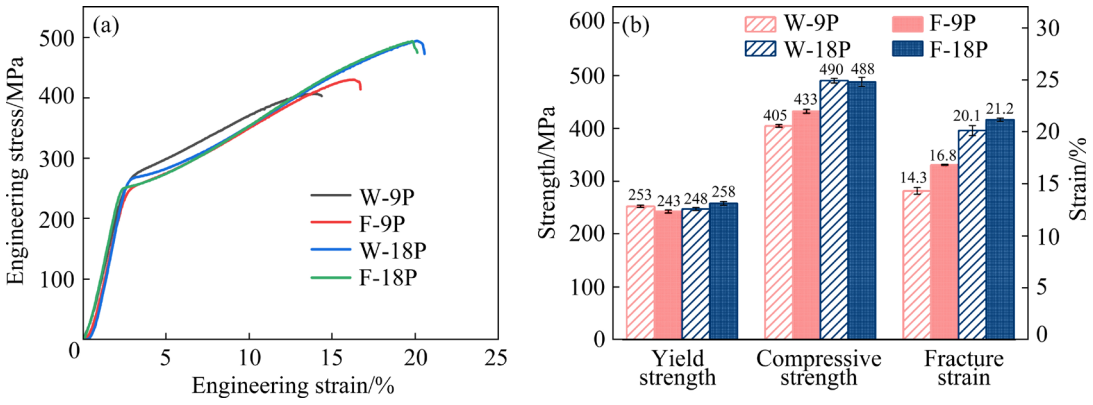

Fig. 9 Engineering stress−strain curves (a) and corresponding statistics (b) of alloys

passes MDF at room temperature. From the curves, it is evident that the mechanical properties are improved significantly with an increase in the number of MDF passes. The bar charts visually demonstrate that the ultimate compressive strength and fracture strain of the samples after 18 passes of MDF show noticeable increases. This can be attributed to the higher degree of DRX in the alloys after 18 passes, resulting in greater homogeneity and a smaller average grain size. Additionally, the larger proportion of recrystallized grains not only contributes to the high strength of the alloy but also enhances its toughness, thereby promoting the ductility.

Moreover, the F alloy exhibits higher volume fraction of DRX and more uniform microstructure, resulting in higher ultimate compressive strength and fracture strain compared to the W alloy. However, because the degree of DRX of F and W alloys after 18 passes is high, the mechanical properties between the W and F alloy are less different. F-18P sample has the best comprehensive mechanical properties, with a yield strength of 258 MPa, an ultimate compressive strength of 488 MPa, and a fracture strain of 21.2%. XIA et al [27] investigated Mg−8.5Gd−4.5Y−0.3Zr (wt.%) alloys with and without Zn addition and found that the alloy with Zn addition has finer grains due to the existence of LPSO phase. It also has high yield strength and elongation, with the elongation and yield strength of the peak-aged alloy with Zn addition being about two times and 56 MPa higher than that of the alloy without Zn addition. In summary, MDF deformation significantly improves the compressive strength and plasticity of the alloy, and the F alloy with LPSO phase has better plasticity.

4 Discussion

4.1 Twin types and quantity differences

Based on the microstructure analysis in Section 3.2, it can be seen that the twinning in the edge region is the most obvious. Therefore, the edge region of the W and F alloys under different forging passes was selected to more accurately analyze the difference in the quantity of activated twins. The fraction of each type of twin boundary to the sum of all large angle boundary lengths was used to characterize the quantity of twins. The results are shown in Fig. 10, where $\{10\bar{1}2\}$ tensile twins are the main activated twins in the deformation process, while the other two types of twins are relatively few. This may be caused by two factors: firstly, the critical resolved shear stress (CRSS) required to activate the compression twin is much higher than that required for the tensile twin [28]. Secondly, tensile twins mainly occur at the early stage of deformation to coordinate the deformation [29,30], while compression twins mainly occur at the late stage of deformation to coordinate the stress concentration [31]. Therefore, the 9 passes deformation of the edge region may result in a small quantity of compression twins due to insufficient stress concentration.

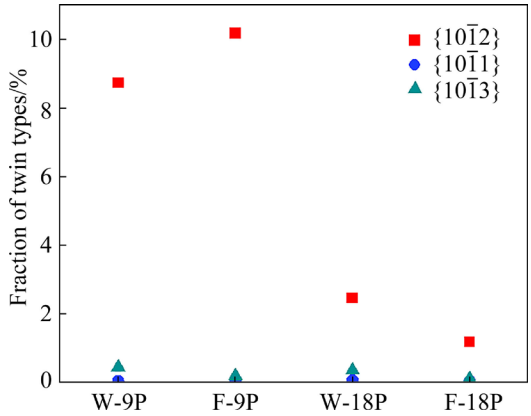

Fig. 10 Fraction of different twin types of alloys with different passes of MDF

Besides, the quantity of twins in the microstructure after 18 passes is less than that after 9 passes. This is because, under the condition of 18 passes, although the strain amount is large, it is easy to activate the twins. However, DRX releases part of the stress concentration, which is also not conducive to the activation of compression twin. There is a large number of twins after 9 passes deformation of F and W alloys, so it can be considered that twinning plays an important role in deformation. The occurrence of twinning deflects the matrix at a certain angle, making the deformation orientation change to a soft orientation, which is conducive to subsequent deformation. By comparing the twinning behavior of W and F alloys, it can be found that the presence of LPSO phase promotes the activation of $\{10\bar{1}2\}$ tensile twins at the initial stage of MDF. However, with the progress of MDF, LPSO phase promotes DRX, releases the stress concentration, and thus reduces the quantity of $\{10\bar{1}2\}$ tensile twins.

Although $\{10\bar{1}2\}$ tension twins are the main types of activated twins, there are still a small number of other types of twins. In order to further understand the influence of the occurrence of different types of twins on crystal orientation, the region with obvious twinning behavior is selected for in-depth analysis based on EBSD data. As shown in Fig. 11, only grains with twinning are marked in the figure, and the orientations of matrix and twins are shown by hexagonal prisms in Figs. 11(a, d). According to the IPF color of the twins and the corresponding scatter plot distribution of {0001}, it can be seen that there are two types of twins in Fig. 11(a). Figure 11(c) shows the angle distribution of point-to-point misorientation between L1 and L2 in Fig. 11(a). It can be seen that the corresponding misorientations between the two large angle interfaces along L1 are 85.4° and 86.2° respectively, and the rotation axis is $[\bar{2}110]$, which is consistent with the $\{10\bar{1}2\}$ tensile twinning. Therefore, T1 twin marked by L1 should be a $\{10\bar{1}2\}$ tensile twin. As can be seen from the misorientation distribution along L2, the corresponding misorientations of the two large angle interfaces are 58.1° and 56.4° respectively, and the rotation axes are $[\bar{2}110]$ and $[2\bar{1}\bar{1}0]$. Therefore, T2 twin marked by L2 should be $\{10\bar{1}1\}$ compression twin. By the same method, the type of T3 twin marked by L3 is $\{10\bar{1}3\}$ compression twin.

4.2 Kink coordination deformation

4.2.1 Kink of coarse grain

Previous studies [32−35] have shown that the LPSO phase inhibits the initiation of slip and twinning in rare earth (RE) magnesium alloys. As a result, Mg−RE alloys containing LPSO phase exhibit a higher tendency for kinking deformation. Figure 12 presents the EBSD results of the kink in the original coarse grain of the W alloy after MDF deformation. Black regions can be observed between different IPF color parts, which indicates the presence of dislocation walls formed by the accumulation of numerous dislocations, as proposed by HESS and BARRETT [36]. These dislocation walls result in localized stress concentration, which is difficult to be captured by EBSD and is represented as black regions. The kink grains are labeled as Regions 1−8, with each hexagonal prism representing the orientation of its corresponding region. The different IPF colors of each part indicate a change in the orientation relationship among them. Grains labeled 1, 3, 5, and 7 exhibit almost the same orientation, indicating that the $\langle 11\bar{2}0\rangle$ crystal orientation is parallel to the LD direction. By examining the hexagonal prism orientation of the kinked grains, it can be inferred that the change in orientation is dependent on the deflection of the *a* and *c* axes. The {0001} pole diagram in Fig. 12(b) further illustrates that the formation of kink band leads to a

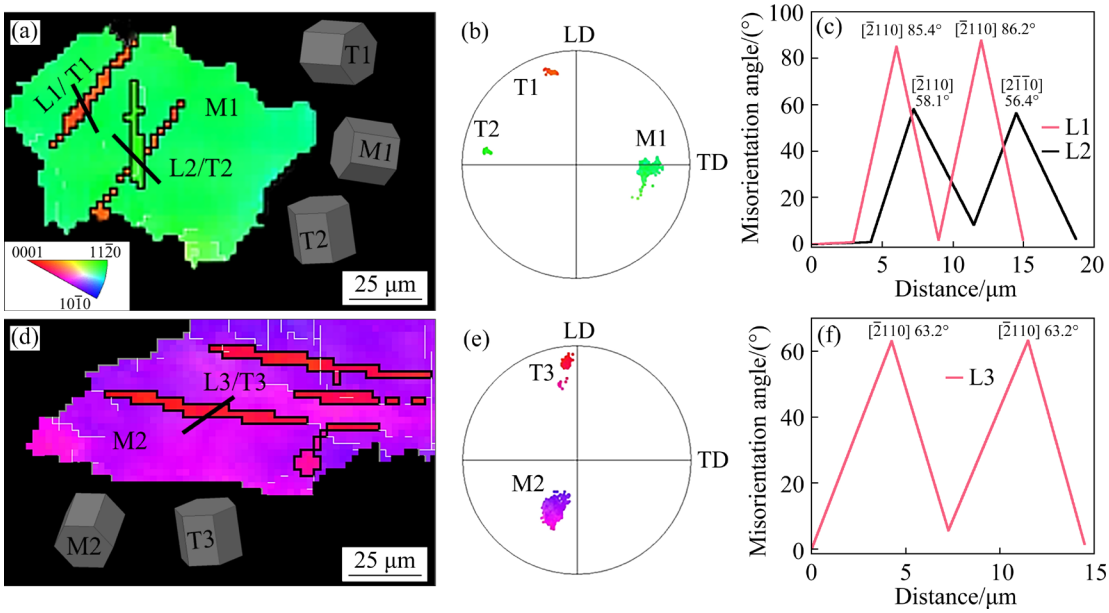

Fig. 11 Twins activated during MDF: (a, d) IPF maps; (b, e) {0001} scatter pole figures; (c, f) Misorientation distribution: (a−c) T1 and T2 twins: (d−f) T3 twin

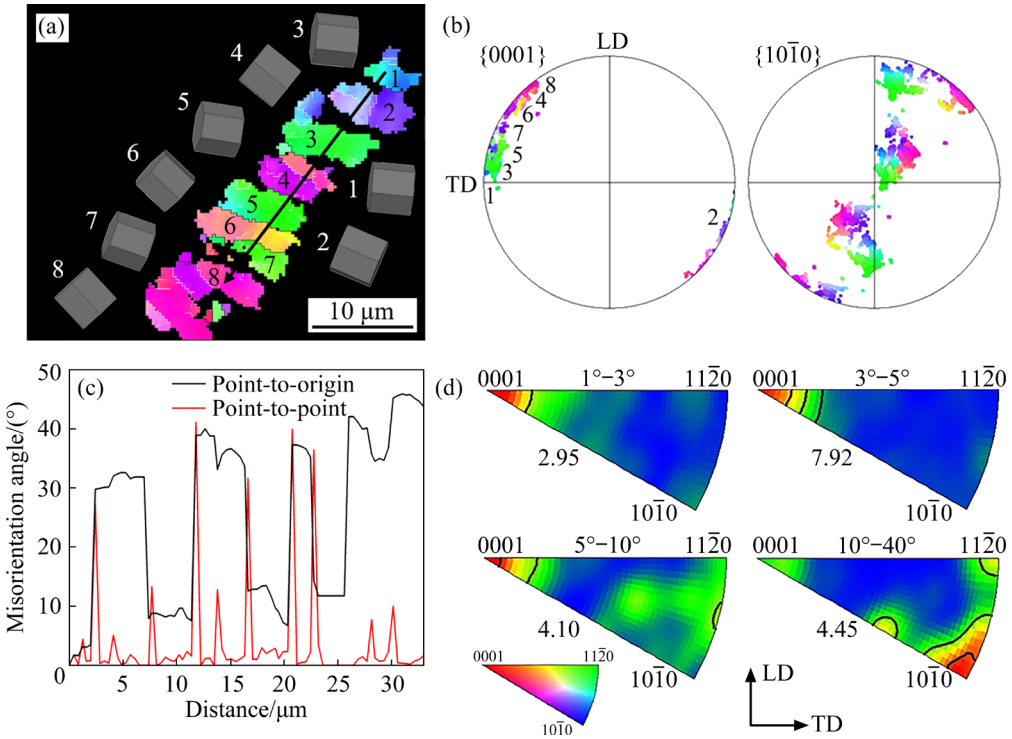

Fig. 12 EBSD results of kink band: (a) IPF map; (b) {0001} and {10$\bar{1}$0} scatter pole figures; (c) Misorientation angle distribution; (d) IGMA

deflection in the orientation of the matrix. Each region exhibits a different deflection direction and angle, resulting in a zonal distribution in the {0001} and {10$\bar{1}$0} pole figures. Consequently, during the MDF deformation of initial large grains, the deformation of each grain part varies due to the non-uniform internal forces acting on the grains under external loads. The low-angle grain boundaries are formed among the parts of non-uniform deformation grains, and these low-angle grain boundaries are continuously deflected into high-angle grain boundaries under the load.

Figure 12(d) shows the in-grain misorientation axes distribution (IGMA) in the kink region. The type of IGMA at the interface of the kink band is related to the type of dislocations at its interface [37]. According to the research results of CHUN et al [38], preferred distribution of IGMA can be considered only when the maximum polar density value is greater than 2. When the maximum polar density value is less than 2, the IGMA is considered to be randomly distributed. In the figure, it can be observed that the IGMA below 10° is concentrated in the ⟨0001⟩ crystal direction, with a polar density value greater than 2. The IGMA above 10° is concentrated in the ⟨10$\bar{1}$0⟩ crystal direction, also with a polar density value greater than 2. The IGMA of the kink band formed by the dislocations of the basal plane is generally distributed in the direction of ⟨10$\bar{1}$0⟩, ⟨10$\bar{2}$0⟩ or the vector superposition of both (commonly referred to as ⟨*uvt*0⟩) [39]. YAMASAKI et al [37] found in kink deformation that the kink band caused by the start-up of prismatic slip was the prismatic ⟨*a*⟩ dislocation on the interface, and the orientation change caused by the kink band was the rotation of the matrix around the *c* axis. Based on the above analysis, it can be concluded that the formation of the kink involves both basal plane rotation and prismatic rotation. According to the point-to-point misorientation distribution in Fig. 12(c), it can be observed that the misorientation between each part of the kink is generally greater than 10°, indicating that the formation of the kink is primarily caused by the rotation of the basal plane.

4.2.2 Kink of LPSO phase

Similarly, Fig. 13 shows the characteristic of kinking in the F alloy. Figure 13(a) shows the EBSD results of the kinked grains, which display noticeable orientation changes. The grains are divided into Regions 1−6 based on their different orientations. By examining the hexagonal prisms, it

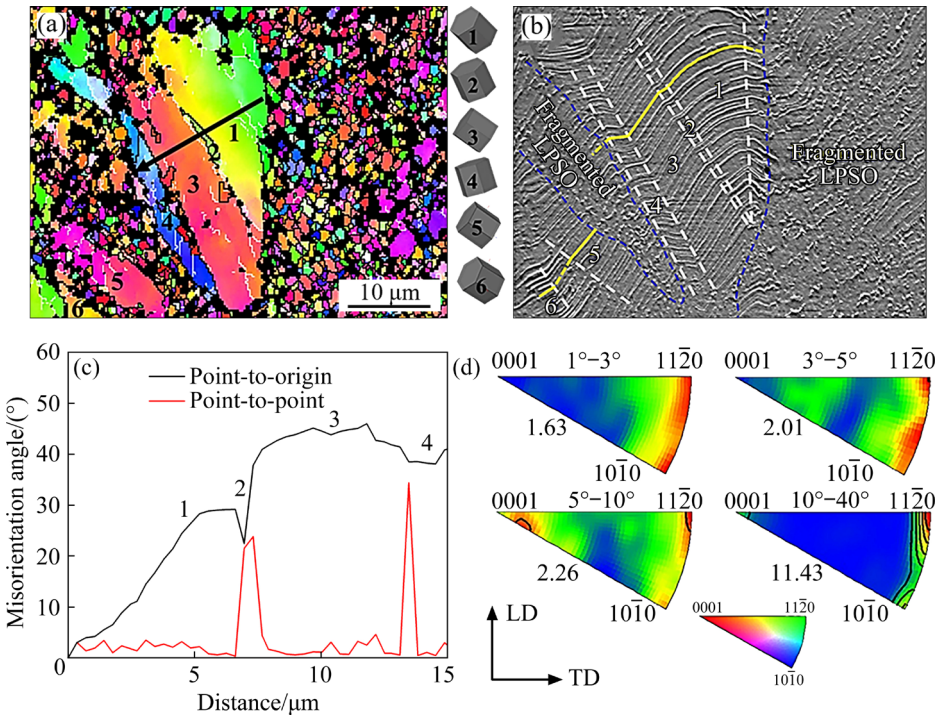

Fig. 13 EBSD results of kink band: (a) IPF map; (b) SEM image of kink area; (c) Misorientation angle distribution; (d) IGMA

can be observed that the orientation changes in each region are attributed to simultaneous rotations of the *a* and *c* axes. Figure 13(b) shows the SEM image of the kinked area in Fig. 13(a). The black contrast represents the magnesium matrix, while the white contrast corresponds to the Zn and Gd elements with higher relative molecular masses. Bright white needle-like LPSO phases can be clearly observed in the image. These LPSO phases have experienced kinking at several locations during the MDF process. The dotted lines in the figure mark the kink interfaces. It can be noticed that the distribution directions of the LPSO phases on both sides of the same kink interface are opposite. Some kinked LPSO phases exhibit a broken and discontinuous distribution, and they disappear in the regions of recrystallized grains. The disappearance of the LPSO phase may be associated with the recrystallization behavior.

Figure 13(c) illustrates the misorientation relative to the point-to-point and point-to-initial-point within the region indicated by the black arrow in Fig. 13(a). The misorientation gradually increases within Region 1, while Regions 3 and 4 exhibit minimal changes in misorientation. Between Regions 1 and 3, there is a small Region 2 enclosed by two high-angle grain boundaries (misorientation larger than 15°). By comparing this with the kink interface depicted in Fig. 13(b), it can be inferred that this small area is formed by kinking. Figure 13(d) shows the distribution of IGMA in the kink region. No significant concentrated distribution is observed for misorientations below 3°, while rotation axis of misorientations above 3° is concentrated in the crystal direction ⟨11$\bar{2}$0⟩, with a polar density value greater than 2. Therefore, this kink corresponds to the basal plane kink type, and its formation is closely associated with the motion of basal plane dislocations.

4.3 DRX behaviors during MDF process

4.3.1 DRX associated with kinking of LPSO phases

Figure 14 shows the bright-field image of microstructure in the center region (with a relatively high degree of recrystallization) of the F alloy after 9 passes of MDF. As shown in Fig. 14(a), there are two different kink interfaces of LPSO phase. In one case, the LPSO phase is distributed coherently at the kink interface, and the kink deformation only changes its distribution direction. In the other case, the LPSO phase breaks at the kink interface. The kink deformation changes the distribution direction

of the LPSO phase, and the LPSO phase is discontinuous at the kink interface, as shown in the black dotted box area in Fig. 14(a). These two types of kink interfaces are related to the degree of stress concentration. If the degree of stress concentration at the kink interface is relatively weak, the LPSO phase may only have a small angle deviation without fracturing at the kink interface. If the stress concentration at the kink interface is strong, the LPSO phase is more likely to kink and break, resulting in the discontinuous distribution of the LPSO phase at the kink interface. This can be clearly observed in Fig. 14(a), where DRX nucleation (marked by black arrows and red dotted lines) occurs near the fragmented LPSO phase. The fragmented lamellar LPSO phase promotes the DRX nucleation through the particle-stimulated nucleation (PSN) mechanism [40].

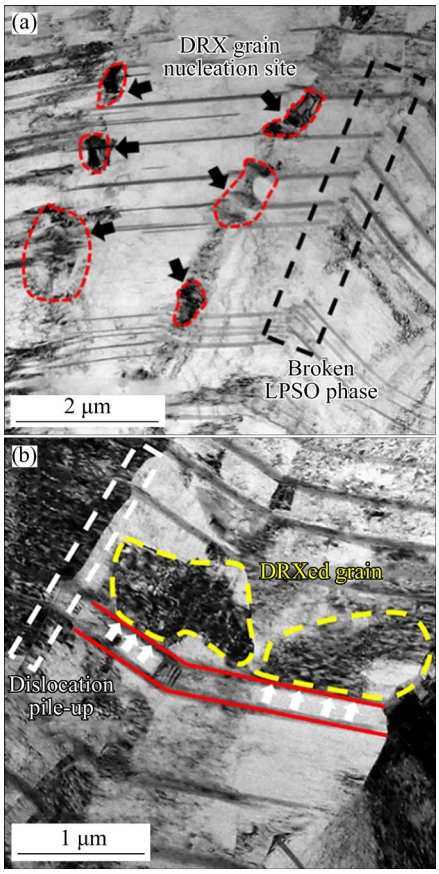

Fig. 14 Bright field images of dynamic recrystallization at kink interface in F-9P alloy

As shown in Fig. 14(b), the distribution of dislocations in the microstructure is inhomogeneous, and the density of dislocations piling up at the kinked interface of the LPSO phase is greater than that in the LPSO phase lamellae, as indicated by the white dotted area in the figure. Additionally, fine subcrystals (marked by the yellow dotted lines, approximately 1 μm) are observed at the kinked interface of the LPSO phase. There is a contrast difference between these subcrystals and the matrix under the bright field image, indicating that the orientation of these subcrystals is deflected relative to the matrix. It is suggested that these fine subcrystals are formed by DRX during the thermal deformation process. ZHU et al [41] observed similar DRX grains in extruded 85.8Mg−7.1Y−7.1Ni (at.%) alloy and equal channel angular extruded 85.8Mg−7.1Y−7.1Zn (at.%) alloy, and proposed that the DRX containing LPSO phase structure occurs locally near the grain boundary with strong stress concentration during extrusion. As shown in Fig. 14, high density dislocations accumulate in these deformation regions, especially at the kink interface. The rearrangement of these dislocations leads to dynamic recovery and DRX during thermal deformation. CHEN et al [42] studied the MDF process of homogenized Mg−2.36Y−0.98Zn (at.%) alloy containing LPSO phase and found that the areas filled with kinked LPSO phase are potential sites that favor the initiation of DRX. Therefore, DRX may preferentially occur in the distorted or heavily curved regions of the LPSO phase.

4.3.2 Effect of interaction of temperature and LPSO phase on DRX behaviors

The experimental results in Section 4.3.1 show that the fragmented lamellar LPSO phase promotes the nucleation of DRX in the alloy during the MDF process. It is also observed that the presence of the lamellar LPSO phase affects the growth of DRX grains in the F alloy. Figure 15 presents the TEM observation results of the F alloy after MDF deformation. In Fig. 15(a), it can be seen that the grain boundary of the recrystallized grain is parallel to the orientation of the lamellar LPSO phase. It is observed that the expansion of the recrystallized grain is hindered by the lamellar LPSO phase. Additionally, in Fig. 15(b), the grain boundary of the recrystallized grain is perpendicular to the orientation of the lamellar LPSO phase, and the grain boundaries of DRX grains recess inward. This indicates that the lamellar LPSO phase hinders the expansion of recrystallized grains. Therefore, lamellar LPSO phase has an obstruction effect on the growth of recrystallized grains.

Figure 16 presents the IPF maps of W alloy and F alloy after 18 passes of MDF at 500 °C, along with the corresponding statistical diagram of grain size and the misorientation angle distribution maps. The high-angle grain boundaries (HAGBs, θ>15°) and the low-angle grain boundaries (LAGBs, 3°≤θ<15°) are noted by black lines and white lines, respectively. The average grain size of W alloy is 1.21 μm, while that of the F alloy is 1.55 μm. This suggests that the recrystallized grain size of the F alloy is slightly larger than that of the W alloy under the same deformation condition. Based on the previous analysis, it can be inferred that the presence of LPSO phase promotes the DRX during the deformation process. Consequently, the formation of DRX grains occurs earlier in the F alloy compared to the W alloy, and these initial DRX grains continue to grow with increasing temperature.

Meanwhile, it can be observed from Figs. 16(c, f) that the volume fractions of LAGBs in the W and F alloys are 40.68% and 22.71%, respectively. During the early stage of deformation, the basal and non-basal dislocations become entangled and rearrange to form LAGBs or subgrain boundaries. As the deformation progresses, new dislocations generated by LAGBs are gradually absorbed into HAGBs. Eventually, the HAGBs migrate to form equiaxed recrystallized grains. Therefore, the smaller volume fraction of LAGBs in the F alloy suggests a more severe DRX through the continuous dynamic recrystallization

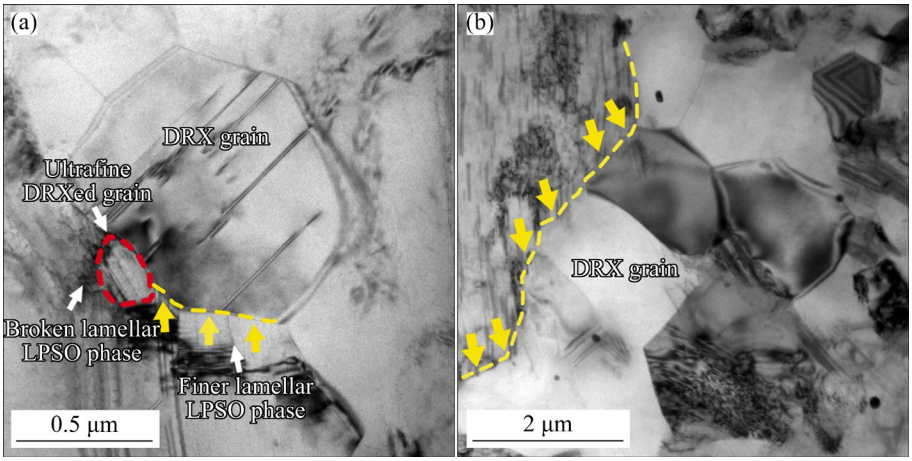

Fig. 15 Bright field images of dynamic recrystallization grains in F alloy

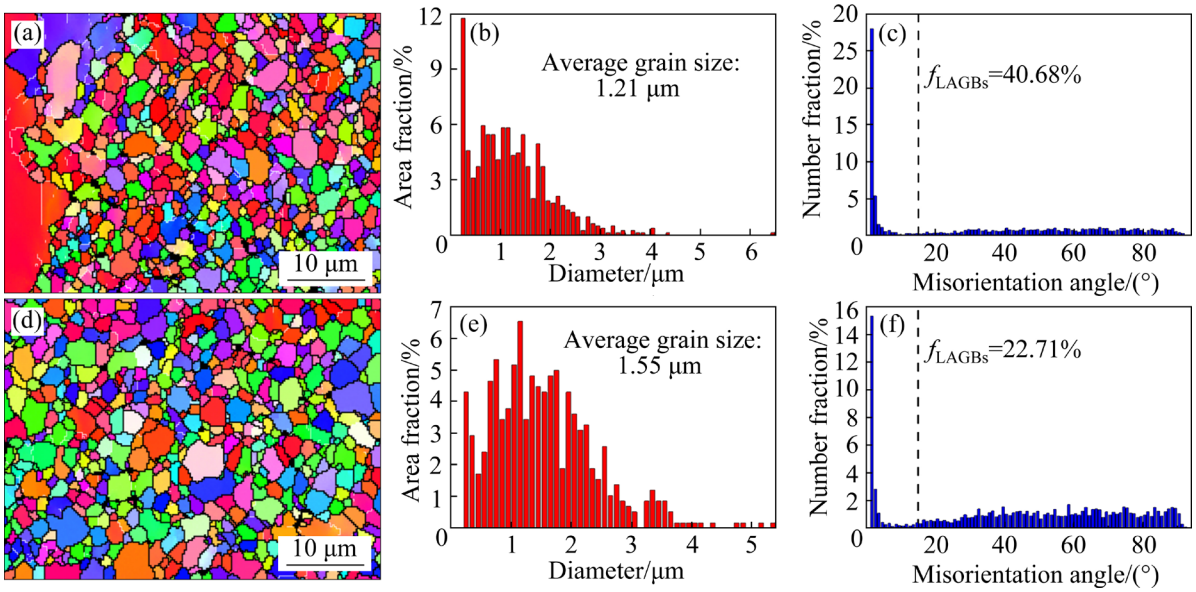

Fig. 16 IPF maps of center region microstructure (a, d), dynamic recrystallization grain size distribution maps (b, e) and grain boundary misorientation maps (c, f): (a−c) W-T500-18P alloy; (d−f) F-T500-18P alloy

(CDRX) mechanism [43,44]. In summary, although the LPSO phase inhibits the growth of recrystallized grains, the effect of deformation temperature on recrystallized grain growth is much greater than the effect of LPSO phase. Consequently, the F alloy exhibits the largest DRX grain size after 18 passes of MDF at 500 °C.

5 Conclusions

(1) During the early stage of the MDF process, twinning occurs in most grains and dynamic recrystallization (DRX) is induced at grain boundaries. The degree of recrystallization is found to be the highest in the center region, and the furnace-cooled alloy containing LPSO phase exhibits a higher degree of recrystallization.

(2) The furnace-cooled alloy after 18 passes of MDF exhibits the best comprehensive mechanical properties, with a yield strength of 258 MPa, ultimate compressive strength of 488 MPa, and fracture strain of 21.2%. MDF deformation significantly improves the ultimate compressive strength and fracture strain, and the furnace-cooled alloy with LPSO phase shows better plasticity.

(3) A large number of crisscross $\{10\bar{1}2\}$ tensile twins are observed within the original coarse crystals during MDF. Additionally, kink also plays an important role in MDF process. The fragmented lamellar LPSO phase at the kink interface promotes the nucleation of DRX through the particle-stimulated nucleation mechanism, but the lamellar LPSO phase inhibits the growth of DRX grains.

(4) The microstructure of the homogenized alloy is significantly refined by MDF deformation, and the grain refinement is mainly affected by the degree of recrystallization. After 18 passes of MDF, the average grain size of the fine recrystallized grains in the center region is about 1−2 μm.

CRediT authorship contribution statement

Jing-yi HUANG: Investigation, Data curation, Writing − Original draft; **Yao-ling LIU:** Investigation, Data curation; **Yu-xiang HAN:** Writing − Review & editing; **Ying-chun WAN:** Supervision; **Chu-ming LIU:** Validation, Resources; **Zhi-yong CHEN:** Writing − Review & editing, Supervision.

Declaration of competing interest

The authors declare that they have no known competing financial interests or personal relationships that could have appeared to influence the work reported in this paper.

Acknowledgments

The authors are grateful for the financial supports from the Key Research and Development Program of Hunan Province, China (No. 2023GK2020).

References

[1] MORDIKE B L, EBERT T. Magnesium: Properties−applications−potential [J]. Materials Science and Engineering A, 2001, 302: 37−45.

[2] JOOST W J, KRAJEWSKI P E. Towards magnesium alloys for high-volume automotive applications [J]. Scripta Materialia, 2017, 128: 107−112.

[3] ZHANG Kun-ming, QIN Chen, SHE Jia, JING Xue-rui, PENG Peng, TANG Ai-tao, RASHAD M, PAN Fu-sheng. Simultaneous improvement in strength and ductility of extruded Mg alloy via novel closed forging extrusion [J]. Transactions of Nonferrous Metals Society of China, 2022, 32: 2866−2876.

[4] FAN Wen-xue, BAI Yu, LI Guang-yang, CHANG Xing-yang, HAO Hai. Enhanced mechanical properties and formability of hot-rolled Mg−Zn−Mn alloy by Ca and Sm alloying [J]. Transactions of Nonferrous Metals Society of China, 2022, 32: 1119−1132.

[5] XU Qiong, MA A, SALEH B, LI Yu-hua, YUAN Yu-chun, JIANG Jing-hua, NI Chao-ying. Enhancement of strength and ductility of SiC_p/AZ91 composites by RD-ECAP processing [J]. Materials Science and Engineering A, 2020, 771: 138579.

[6] ALI Y, QIU Dong, JIANG Bin, PAN Fu-sheng, ZHANG Ming-xing. Current research progress in grain refinement of cast magnesium alloys: A review article [J]. Journal of Alloys and Compounds, 2015, 619: 639−651.

[7] ALANEME K K, OKOTETE E A. Enhancing plastic deformability of Mg and its alloys—A review of traditional and nascent developments [J]. Journal of Magnesium and Alloys, 2017, 5: 460−475.

[8] ZHANG Yu, WU Yu-juan, PENG Li-ming, FU Peng-huai, HUANG Fei, DING Wen-jiang. Microstructure evolution and mechanical properties of an ultra-high strength casting Mg−15.6Gd−1.8Ag−0.4Zr alloy [J]. Journal of Alloys and Compounds, 2014, 615: 703−711.

[9] SUN Yue-hua, WANG Ri-chu, PENG Chao-qun, WANG Xiao-feng. Effect of Gd on microstructure, mechanical properties, and corrosion behavior of as-homogenized Mg−8Li−3Al−2Zn−0.2Zr alloy [J]. Transactions of Nonferrous Metals Society of China, 2022, 32: 2494−2509.

[10] WANG Chong, LI Hong-rui, GUO En-yu, WANG Xue-jian, KANG Hui-jun, CHEN Zong-ning, WANG Tong-min. The effect of Gd on the microstructure evolution and mechanical properties of Mg−4Zn−0.6Ca alloy [J]. Materials Science and Engineering A, 2023, 868: 144756.

[11] NIE Jian-feng. Precipitation and hardening in magnesium alloys [J]. Metallurgical and Materials Transactions A, 2012, 43: 3891−3939.

[12] NIE Jian-feng, GAO Xiang, ZHU Su-ming. Enhanced age hardening response and creep resistance of Mg−Gd alloys containing Zn [J]. Scripta Materialia, 2005, 53: 1049−1053.

[13] NIE Jian-feng, OH-ISHI K, GAO Xiang, HONO K. Solute segregation and precipitation in a creep-resistant Mg−Gd−Zn alloy [J]. Acta Materialia, 2008, 56: 6061−6076.

[14] PENG Yong-gang, DU Zhi-wei, LIU Wei, LI Yong-jun, LI Ting, HAN Xiao-lei, MA Ming-long, PANG Zheng, YUAN Jia-wei, SHI Guo-liang. Evolution of precipitates in Mg−7Gd−3Y−1Nd−1Zn−0.5Zr alloy with fine plate-like 14H-LPSO structures aged at 240 °C [J]. Transactions of Nonferrous Metals Society of China, 2020, 30: 1500−1510.

[15] WANG Wei-zhen, ZHANG Meng-meng, YANG Zhuo-qun, HU Wei-wei. Dynamic precipitation and strengthening in a Mg−Zn−Gd alloy during hot deformation [J]. Journal of Alloys and Compounds, 2022, 905: 164219.

[16] LUAN Shi-yu, ZHANG Lei, CHEN Li-jia, LI Wei, WANG Jin-hui, JIN Pei-peng. The influence of the LPSO on the deformation mechanisms and tensile properties at elevated temperatures of the Mg−Gd−Zn−Mn alloys [J]. Journal of Materials Research and Technology, 2023, 23: 6216−6229.

[17] ZHANG Jing-huai, LIU Shu-juan, WU Rui-zhi, HOU Le-gan, ZHANG Mi-lin. Recent developments in high-strength Mg-RE-based alloys: Focusing on Mg−Gd and Mg−Y systems [J]. Journal of Magnesium and Alloys, 2018, 6: 277−291.

[18] TORBATI-SARRAF S A, LANGDON T G. Properties of a ZK60 magnesium alloy processed by high-pressure torsion [J]. Journal of Alloys and Compounds, 2014, 613: 357−363.

[19] ZHAN Mei-yan, ZHANG Wei-wen, ZHANG Da-tong. Production of Mg−Al−Zn magnesium alloy sheets with ultrafine-grain microstructure by accumulative roll-bonding [J]. Transactions of Nonferrous Metals Society of China, 2011, 21: 991−997.

[20] CHEN Qiang, SHU Da-yu, HU Chuan-kai, ZHAO Zu-de, YUAN Bao-guo. Grain refinement in an as-cast AZ61 magnesium alloy processed by multi-axial forging under the multitemperature processing procedure [J]. Materials Science and Engineering A, 2012, 541: 98−104.

[21] JAHADI R, SEDIGHI M, JAHED H. ECAP effect on the micro-structure and mechanical properties of AM30 magnesium alloy [J]. Materials Science and Engineering A, 2014, 593: 178−184.

[22] TANG Wan-ru, LIU Shi-meng, LIU Zheng, KANG Shuang, MAO Ping-li, ZHOU Le, WANG Zhi. Microstructure evolution and constitutive relation establishment of Mg−7Gd−5Y−1.2Nd−0.5Zr alloy under high strain rate after severe multi-directional deformation [J]. Materials Science and Engineering A, 2021, 809: 140994.

[23] JAMALI A, MAHMUDI R. Evolution of microstructure, texture, and mechanical properties in a multi-directionally forged ZK60 Mg alloy [J]. Materials Science and Engineering A, 2019, 752: 55−62.

[24] WANG Bi-zheng, LIU Chu-ming, GAO Yong-hao, JIANG Shu-nong, CHEN Zhi-yong, LUO Zhen. Microstructure evolution and mechanical properties of Mg−Gd−Y−Ag−Zr alloy fabricated by multidirectional forging and ageing treatment [J]. Materials Science and Engineering A, 2017, 702: 22−28.

[25] LI Kai, CHEN Zhi-yong, CHEN Tao, SHAO Jian-bo, WANG Ren-ke, LIU Chu-ming. Hot deformation and dynamic recrystallization behaviors of Mg−Gd−Zn alloy with LPSO phases [J]. Journal of Alloys and Compounds, 2019, 792: 894−906.

[26] TAHREEN N, ZHANG Ding-fei, PAN Fu-sheng, JIANG Xian-quan, LI Dong-yang, CHEN Dao-lun. Strengthening mechanisms in magnesium alloys containing ternary *I*, *W* and LPSO phases [J]. Journal of Materials Science & Technology, 2018, 34: 1110−1118.

[27] XIA Xiang-sheng, SHU Da-yu, YANG E-chuan, Hu Chuan-kai. A comparative study of the role of Zn in microstructures and the mechanical properties of Mg−Gd−Y−Zr alloys [J]. Journal of Materials Research and Technology, 2023, 25: 2903−2912.

[28] CHRISTIAN J W, MAHAJAN S. Deformation twinning [J]. Progress in Materials Science, 1995, 39: 1−157.

[29] NENE S S, KASHYAP B P, PRABHU N, ESTRIN Y, AL-SAMMAN T. Microstructure refinement and its effect on specific strength and bio-corrosion resistance in ultralight Mg−4Li−1Ca (LC41) alloy by hot rolling [J]. Journal of Alloys and Compounds, 2014, 615: 501−506.

[30] LENTZ M, KLAUS M, BEYERLEIN I J, ZECEVIC M, REIMERS W, KNEZEVIC M. In situ X-ray diffraction and crystal plasticity modeling of the deformation behavior of extruded Mg−Li−(Al) alloys: An uncommon tension−compression asymmetry [J]. Acta Materialia, 2015, 86: 254−268.

[31] LI Lian-hui, LIU Wen-hong, Qi Fu-gang, WU Di, ZHANG Zhi-qiang. Effects of deformation twins on microstructure evolution, mechanical properties and corrosion behaviors in magnesium alloys—A review [J]. Journal of Magnesium and Alloys, 2022, 10: 2334−2353.

[32] SHAO Xiao-hong, YANG Zhi-qing, MA Xiu-liang. Interplay between deformation twins and basal stacking faults enriched with Zn/Y in Mg97Zn1Y2 alloy [J]. Philosophical Magazine Letters, 2014, 94: 150−156.

[33] SHAO Xiao-hong, ZHENG Shi-Jian, CHEN Dong, JIN Qiu-qing, PENG Zhuang-zhuang, MA Xiu-liang. Deformation twinning induced decomposition of lamellar LPSO structure and its re-precipitation in an Mg−Zn−Y alloy [J]. Scientific Reports, 2016, 6: 1−9.

[34] HAGIHARA K, YOKOTANI N, UMAKOSHI Y. Plastic deformation behavior of Mg12YZn with 18R long-period stacking ordered structure [J]. Intermetallics, 2010, 18: 267−276.

[35] MATSUDA M, ANDO S, NISHIDA M. Dislocation structure in rapidly solidified Mg97Zn1Y2 alloy with long period stacking order phase [J]. Materials Transactions, 2005, 46: 361−364.

[36] HESS J B, BARRETT C S. Structure and nature of kink bands in zinc [J]. JOM, 1949, 1: 599−606.

[37] YAMASAKI M, HAGIHARA K, INOUE S, HADORN J P, KAWAMURA Y. Crystallographic classification of kink

bands in an extruded Mg−Zn−Y alloy using intragranular misorientation axis analysis [J]. Acta Materialia, 2013, 61: 2065−2076.

[38] CHUN Y B, DAVIES C H J. Investigation of prism ⟨*a*⟩ slip in warm-rolled AZ31 alloy [J]. Metallurgical and Materials Transactions A, 2011, 42A: 4113−4125.

[39] HAGIHARA K, MAYAMA T, HONNAMI M, YAMASAKI M, IZUNO H, OKAMOTO T, OHASHI T, NAKANO T, KAWAMURA Y. Orientation dependence of the deformation kink band formation behavior in Zn single crystal [J]. International Journal of Plasticity, 2016, 77: 174−191.

[40] HANTZSCHE K, BOHLEN J, WENDT J, KAINER K U, YI Sang-bong, LETZIG D. Effect of rare earth additions on microstructure and texture development of magnesium alloy sheets [J]. Scripta Materialia, 2010, 63: 725−730.

[41] ZHU Su-ming, LAPOVOK R, NIE Jian-Feng, ESTRIN Y, MATHAUDHU S N, Microstructure and mechanical properties of LPSO phase dominant Mg85.8Y7.1Zn7.1 and Mg85.8Y7.1Ni7.1 alloys [J]. Materials Science and Engineering A, 2017, 692: 35−42.

[42] CHEN Tao, CHEN Zhi-yong, SHAO Jian-bo, HAN Yu-xiang, MAO Long-hui, LIU Chu-ming. Fragmentation of long period stacking ordered (LPSO) phase and its impact on microstructure evolution of a Mg−Y−Zn alloy during multi-directional forging [J]. Materials Science and Engineering A, 2020, 793: 139898.

[43] GALIYEV A, KAIBYSHEV R, GOTTSTEIN G. Correlation of plastic deformation and dynamic recrystallization in magnesium alloy ZK60 [J]. Acta Materialia, 2001, 49: 1199−1207.

[44] SITDIKOV O, KAIBYSHEV R. Dynamic recrystallization in pure magnesium [J]. Materials Transactions, 2001, 42: 1928−1937.

含与不含 LPSO 相的 Mg−Gd−Zn 合金多向锻造过程中的显微组织演变及力学性能

黄静怡[1]，刘窈伶[1]，韩宇翔[1]，万迎春[2]，刘楚明[3]，陈志永[1]

1. 中南大学 材料科学与工程学院，长沙 410083；
2. 中南大学 轻合金研究院，长沙 410083；
3. 湖南镁宇科技有限公司，岳阳 414000

摘　要：对 Mg−5.6Gd−0.8Zn (质量分数，%)合金进行均匀化水冷和均匀化炉冷两种热处理工艺，得到无 14H 长周期有序堆积(LPSO)相和有 14H LPSO 相的合金，随后对两种合金进行多向锻造。系统研究了多向锻造过程中合金不同区域(中心、次边部和边部)的显微组织和力学性能，并讨论了 LPSO 相对其影响。结果表明：在多向锻造过程中，合金的晶粒明显细化，各区域形成动态再结晶程度不同的不均匀组织，导致显微硬度的不均匀性；与不含 LPSO 相的合金相比，含 LPSO 相合金的再结晶程度和组织均匀性更高，综合力学性能更好。经 18 道次多向锻造的炉冷态合金的综合力学性能最佳，其抗压强度为 488 MPa，屈服强度为 258 MPa，断裂应变为 21.2%。此外，多向锻造过程中的动态再结晶行为与 LPSO 相和锻造温度密切相关。扭折的 LPSO 相可以作为动态再结晶的潜在形核位点，而破碎的 LPSO 相则通过粒子刺激形核机制促进动态再结晶。

关键词：Mg−Gd−Zn 合金；多向锻造；LPSO 相；孪生；扭折；动态再结晶

(Edited by Bing YANG)